

A new multifractal-based grain size distribution model

Filip Stanić^{a,b,*}, Ioulia Tchiguirinskaia^a, Pierre-Antoine Versini^a, Yu-Jun Cui^b, Pierre Delage^b, Patrick Aïmedieu^c, Ana Maria Tarquis^d, Michel Bornert^c, Daniel Schertzer^a

^a Ecole des Ponts ParisTech, HM&Co, Marne la Vallée, France

^b Ecole des Ponts ParisTech, Navier/CERMES, Marne la Vallée, France

^c Ecole des Ponts ParisTech, Navier/Multi-échelle, Marne la Vallée, France

^d Universidad Politécnica de Madrid (UPM), Dept. of Applied Mathematics, Madrid, Spain

ARTICLE INFO

Handling Editor: Morgan Cristine L.S.

Keywords:

Grain size distribution
Universal multifractals
X-ray computed tomography
Granular media

ABSTRACT

Previous works related to the application of the multifractal theory for analyzing the grain size distribution (GSD), showed the potential of this approach to deal with this complex issue. However, absence of the practical application of this kind of statistical analysis raised some doubts among the soil scientists. Compared to the experimental dry sieving method, which is based on mass representations of different grain sizes, the approach presented in this work relies on the analysis of grain densities (density indicators) scanned by means of X-ray CT (Computed Tomography). By reducing the resolution of the scanned soil image(s), the cumulative representation of solid particles equal to or larger than the actual discretization element can be determined, and described analytically by means of the universal multifractals (UM).

For validation of the new UM approach, the X-ray CT results of three different soils were used: the volcanic substrate covering Green Wave (a green roof of Champs-sur-Marne in France), and two horizons of the soil collected from the low land mountain area of Sierra de Guadarrama in Spain. Comparison between the proposed UM model and the experimental data of these three materials confirms that the GSD can be reasonably well predicted from the scanned images of soils covering wide range of grain sizes. The UM model, unlike the fractal-based models, accounts for fractal dimension that depends on grain size, and hence, based on the preliminary results presented in this work, it could be rather useful in case of multi-modal soils whose GSD curves are described with multiple fractal dimensions.

1. Introduction

The grain size distribution (GSD) is one of the fundamental properties of granular soils that, besides the influence on mechanical characteristics, also affects the packing arrangement of grains (Nolan and Kavanagh, 1993; He et al., 1999 among the others), and hence the distribution of pores that further impacts the hydraulic properties of the porous medium (Segal et al., 2009). Most often the GSD curve is experimentally determined based on the mass fractions of different grain sizes extracted either by using sieves of different void sizes, for grains larger than 80 μm (dry sieving method - AFNOR, 1996), or by means of sedimentation test (AFNOR, 1992; Beuselinck et al., 1998) for finer particles. The alternative approach proposed to measure GSD is a laser diffraction method (Miller and Schaeztl, 2012).

Detailed overview of different approaches used for describing the complexity of GSD curves can be found in Ghanbarian and Hunt (2017).

One of them is the self-similarity principle which is included in fractal-based models and which assumes occurrence of the same pattern of the soil structure at all scales. According to Ghanbarian-Alavijeh et al. (2011), the three-phase PSF (pore-solid-fractal) approach (Perrier et al., 1999; Bird et al., 2000) is the most consistent and with the strongest physical-basis among the fractal-based approaches. Besides pores and grains, it assumes one additional “fictive” type of soil elements – fractals - that are successively broken at smaller scales in a self-similar way, leading finally to the structure consisting of fractal-distributed pore and grain sizes. Thus, the GSD can be represented by means of a power (fractal) law, where the fractal coefficient is included in the exponent. However, unlike assumed in the PSF model, grain densities are non-homogeneous, which also contributes to the complexity of distribution of different mass fractions that often cannot be described with a single fractal dimension (Bittelli et al., 1999).

Multifractal formalism, that takes into account different fractal

* Corresponding author at: Ecole des Ponts ParisTech, HM&Co and CERMES, Marne la Vallée, France.

E-mail address: filip.stanic@enpc.fr (F. Stanić).

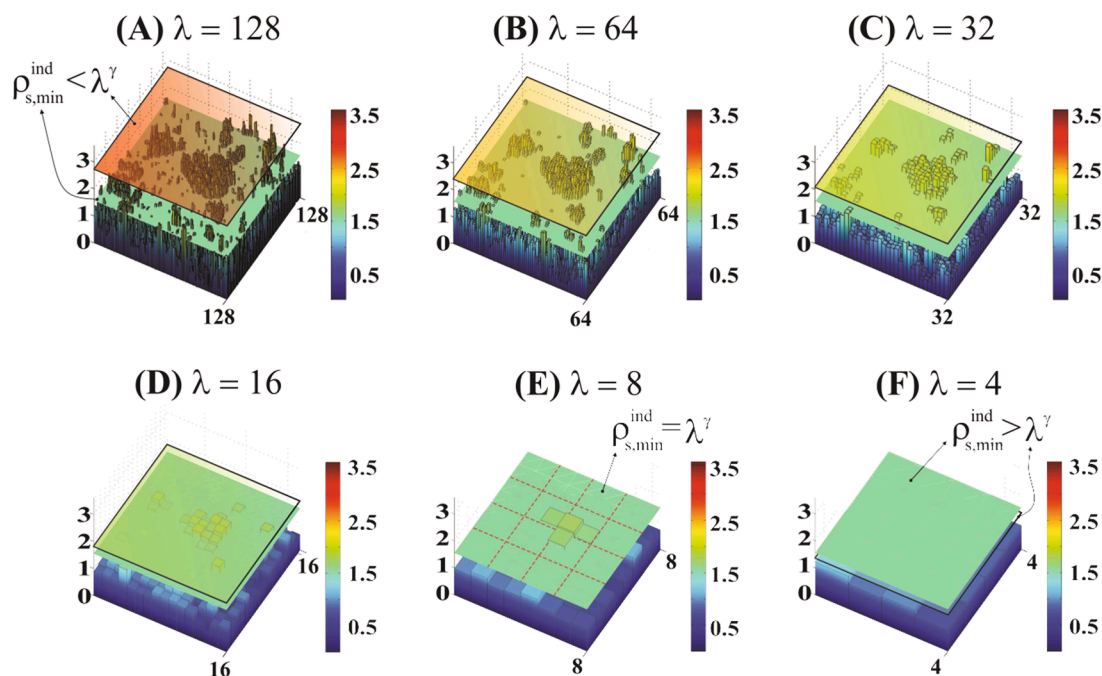


Fig. 1. Change of the two-dimensional $\rho_{s,min}^{ind}(\lambda)$ field with λ at: (A) $\lambda = 128$; (B) $\lambda = 64$; (C) $\lambda = 32$; (D) $\lambda = 16$; (E) $\lambda = 8$; (F) $\lambda = 4$. A turquoise color platform signifies a fixed threshold $\rho_{s,min}^{ind} = 1.55$, while the one with transparent color signifies a resolution dependent threshold λ^γ ($\gamma = 0.211$).

coefficients for different threshold values, was also used for analyzing the complexity of GSD. Grout et al. (1998) and Posadas et al. (2001) used Renyi dimensions, one of the multifractal parameters, to characterize the heterogeneous distribution of different mass fractions. Besides this type of multifractal analysis, the singularity spectra analysis is also applied for analyzing the dry soil volume-size distribution obtained by using a laser distraction method (Martín and Montero, 2002). Recently, Torre et al. (2016) used a X-ray CT, a non-destructive technique for obtaining a three-dimensional grey-scale image of a porous material (Hseih, 2003; Banhart, 2008) in order to compare the three-dimensional structural complexity of spatial arrangement of grains and pores, with that of differently oriented two-dimensional planes. The multifractal analysis has also proved to be convenient in this case. Even though the multifractal theory brings great potential for understanding the complexity of GSD (Ghanbarian and Hunt, 2017), up to date this kind of analysis has not found practical application.

This work is focused on development of a new physically-based GSD model founded on the Universal Multifractal (UM) framework (Schertzer and Lovejoy, 1987, 1997). Based on a grey-scale soil image scanned by means of X-ray CT, it is possible to recognize solid particles of different sizes by progressively decreasing the resolution of the image while keeping the fixed value of the threshold. Change of the representation of solid particles with the resolution of the image can be directly linked with the grain size distribution, and described analytically in a mathematically-elegant way by means of the UM framework. Compared to work of Lai and Chen (2019), where a sophisticated machine learning tool was used for particle recognition, this approach is much simpler and more convenient for practical application.

The UM framework in combination with X-ray CT imaging was firstly validated for some artificial volcanic substrate (Stanić et al., 2020a, 2020b) used for covering green roof named Green Wave (Versini et al., 2018, 2020). Results of the model, whose parameters are directly determined from scanned images, were first compared with the experimental data obtained by means of the standard dry sieving method (AFNOR, 1996) and sedimentation test (AFNOR, 1992). Furthermore, the UM model was tested on scanned images of two horizons of an intact soil sample collected from the low land mountain area of Sierra de Guadarrama (Schmid et al., 2016) called La Herreria. In this case, results

of the model were compared with measured percentages of sand, silt and clay particles, since detailed GSD curves are lacking. Finally, for published experimental GSD data of the GW substrate and Walla Walla soil (Bittelli et al., 1999), the UM model was compared with the fractal-based PSF model.

2. Methodology

The GSD model proposed in this work is based on the recognition of solid particles of different sizes from the scanned soil image, by changing the resolution of the image. This can be described analytically through the application of the Universal Multifractals (UM) framework (Schertzer and Lovejoy, 1987, 1997) which is briefly described below. Note that two-dimensional scanned soil images (Euclidian dimension $E = 2$), extracted from the three-dimensional one ($E = 3$), were analyzed in this work in order to simplify the methodology presented. However, this simplified approach ($E = 2$) is credible only under certain conditions that are described later in the text, while otherwise the same methodology should be applied for $E = 3$.

2.1. Universal multifractal (UM) theoretical framework

In Fig. 1 is presented a renormalized two-dimensional soil density indicator field $\rho_{s,min}^{ind}(\lambda)$ at various resolutions λ , which is, due to the better visualization, presented in a three-dimensional form. Here, $\lambda = \frac{L}{l(\lambda)}$ is equal to the ratio between the size of the image L [L] and the size of a single pixel $l(\lambda)$ [L], representing the number of pixels along an edge of the image. Values of $\rho_{s,min}^{ind}(\lambda) = \rho(\lambda) / \rho_{bulk}$ are presented as histogram at each λ , where ρ_{bulk} is the constant bulk density of the dry material [M/L^3] ($\rho_{s,min}^{ind} = 1$ is a renormalized ρ_{bulk}). Clearly, $\rho_{s,min}^{ind}(\lambda)$ values mitigate as λ decreases by merging pixels in groups by λ_1^2 , where λ_1 is an integer value equal 2 (check dashed gridlines in Fig. 1e). By averaging $\rho_{s,min}^{ind}(\lambda)$ values of each group, attenuated $\rho_{s,min}^{ind}(\lambda)$ field is obtained with λ_1 times smaller λ and λ_1 times larger pixel size $l(\lambda)$.

By means of the UM (Schertzer and Lovejoy, 1987, 1997) it is possible to compute, at different λ , the probability that $\rho_{s,min}^{ind}(\lambda)$ exceeds λ^γ , a renormalized threshold value that changes with λ (a transparent color

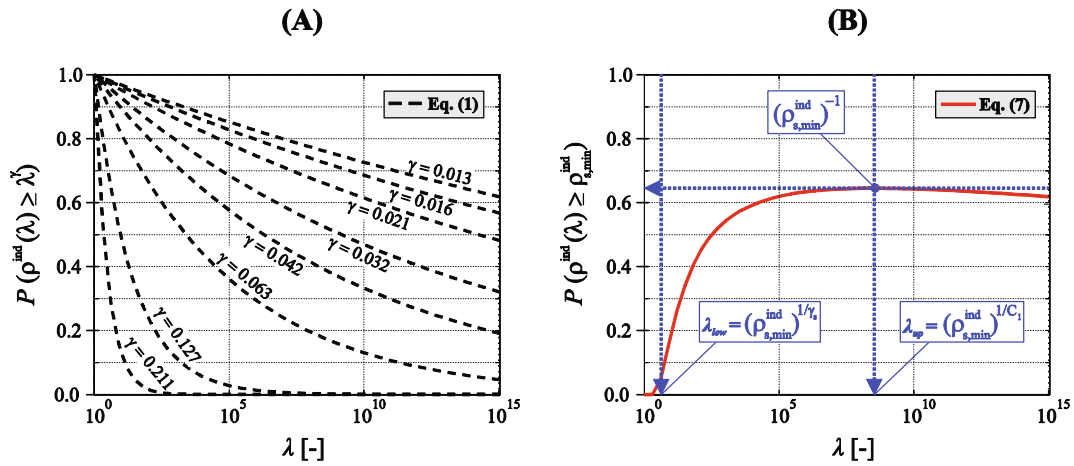


Fig. 2. a) Equation (1) (dashed lines) calculated for: $C_1 = 2.23 \times 10^{-2}$, $\alpha = 1.67$ (values that characterize $\rho^{ind}(\lambda)$ field in Fig. 1) and different values of γ (including $\gamma = 0.211$); b) Eq. (5) (solid line) calculated for the same values of C_1 and α and the fixed value of $\rho_{s,min}^{ind} = 1.55$.

platform in Fig. 1). Threshold value is expressed through the fixed dimensionless singularity γ [-], and therefore it decreases together with λ (see Fig. 1a–f) until it reaches unit value at $\lambda = 1$. For a certain value of γ ($=0.211$ in Fig. 1), the previously mentioned probability of exceeding can be computed as:

$$P(\rho^{ind}(\lambda) \geq \lambda^\gamma) = \frac{N(\rho^{ind}(\lambda) \geq \lambda^\gamma)}{\lambda^E} \approx \lambda^{-c(\gamma)} \quad (1)$$

$$c(\gamma) = C_1 \left(\frac{\gamma}{C_1 \alpha} + \frac{1}{\alpha} \right)^\alpha; \alpha' = \left(1 - \frac{1}{\alpha} \right)^{-1}, \alpha \neq 1 \quad (2)$$

where $N(\rho^{ind}(\lambda) \geq \lambda^\gamma)$ is the number of $\rho^{ind}(\lambda)$ values that are equal to or higher than λ^γ , while $c(\gamma)$ is the co-dimension function that, besides γ , depends on two parameters, C_1 and α . Note that in Eq. (1) an approximate equal sign is used because term $\frac{N(\rho^{ind}(\lambda) \geq \lambda^\gamma)}{\lambda^E}$ is computed by counting $N(\rho^{ind}(\lambda) \geq \lambda^\gamma)$ at different λ (discrete form), while $\lambda^{-c(\gamma)}$ is related to the UM analytical form.

Parameters C_1 and α fully characterize ρ^{ind} field, where C_1 describes the sparseness of the mean value of the field while α describes the change of sparseness for values around the mean. As explained in Schertzer and Lovejoy (1987), C_1 takes values between 0 (mean value is ubiquitous - homogeneous field) and E (mean value is too sparse to be observed), while α takes values between 0 (no occurrence of extremes - fractal field) and 2 (maximal occurrence of extremes - log-normal field). Equation (1) is presented in Fig. 2a for $C_1 = 2.23 \times 10^{-2}$ and $\alpha = 1.67$, values that characterize $\rho^{ind}(\lambda)$ field in Fig. 1, and different γ values (including $\gamma = 0.211$) corresponding to various dashed lines.

2.2. Adaptation of the UM framework – New GSD model

In this work, the presented up-scaling procedure is used for recognizing solid particles of different sizes from the obtained $\rho^{ind}(\lambda)$ field. Compared to the previous explanation, where a resolution dependent threshold λ^γ was accounted for, here is used a fixed threshold value $\rho_{s,min}^{ind}$ (solid platform in Fig. 1) related to the renormalized minimal grain density ($\rho_{s,min}^{ind} > 1$). Therefore, $\rho^{ind} \geq \rho_{s,min}^{ind}$ values indicate the total area of the image covered with solid particles (grains). As shown in Fig. 1, this area reduces when up-scaling, mostly by getting rid of isolated $\rho^{ind}(\lambda) \geq \rho_{s,min}^{ind}$ values that are surrounded by those lower than $\rho_{s,min}^{ind}$. On the contrary, larger continuous zones covered by $\rho^{ind}(\lambda) \geq \rho_{s,min}^{ind}$ values resist longer to the up-scaling process, indicating the presence of a large grain on that location (central zone in Fig. 1). Therefore, the total area covered with $\rho^{ind}(\lambda) \geq \rho_{s,min}^{ind}$ values at certain λ indicates a cumulative

representation of solid particles of diameter equal to or larger than the size of a single pixel $l(\lambda) = L/\lambda$:

$$P(\rho^{ind}(\lambda) \geq \rho_{s,min}^{ind}) = \frac{N(\rho^{ind}(\lambda) \geq \rho_{s,min}^{ind})}{\lambda^E} \quad (3)$$

In order to transform Eq. (3) into the distribution function $P(d \geq l(\lambda))$, it is necessary to renormalize it with respect to the initial representation of solid particles met at $\lambda_n \leq \lambda_{up}$. Therefore, $P(d < l(\lambda)) = 1 - P(d \geq l(\lambda))$ can be expressed as:

$$P(d < l(\lambda)) = 1 - \frac{P(\rho^{ind}(\lambda) \geq \rho_{s,min}^{ind})}{P(\rho^{ind}(\lambda_n) \geq \rho_{s,min}^{ind})} = 1 - \frac{N(\rho^{ind}(\lambda) \geq \rho_{s,min}^{ind})}{N(\rho^{ind}(\lambda_n) \geq \rho_{s,min}^{ind})} \left(\frac{\lambda_n}{\lambda} \right)^E \quad (4)$$

The analogy between Eq. (4) and the dry sieving method is explained in the Appendix. Equation (3), and hence Eq. (4), can be described analytically through the UM framework if expressing $\rho_{s,min}^{ind}$, which is independent on λ , through λ :

$$\rho_{s,min}^{ind} = \frac{\rho_{s,min}}{\rho_{bulk}} = \lambda^{\gamma(\lambda)} \quad (5)$$

where $\rho_{s,min}$ is the minimal grain density [M/L^3], and $\gamma(\lambda)$ differs from a fixed γ used in Eqs. (1) and (2), since it changes with λ in order to maintain fixed value of $\rho_{s,min}^{ind}$:

$$\gamma(\lambda) = \frac{\ln(\rho_{s,min}^{ind})}{\ln(\lambda)} \quad (6)$$

Finally, by introducing Eq. (6), instead of γ , into Eq. (2), it is possible to express Eq. (3) analytically:

$$P(\rho^{ind}(\lambda) \geq \rho_{s,min}^{ind}) \approx \lambda^{-c(\gamma(\lambda))} = \lambda^{-C_1 \left(\frac{\ln(\rho_{s,min}^{ind})}{\ln(\lambda)} \frac{1}{C_1 \alpha} + \frac{1}{\alpha} \right)^\alpha} \quad (7)$$

Equation (7) is presented in Fig. 2b with solid line which is also fully characterized by means of parameters C_1 and α . Value of $\gamma(\lambda) = C_1$ corresponds to the upper resolution limit $\lambda_{up} = (\rho_{s,min}^{ind})^{1/C_1}$ (see Eq. (6)) for which, due to the fact that $c(\gamma(\lambda) = C_1) = C_1$ (see Eq. (2)), $P(\rho^{ind}(\lambda) \geq \rho_{s,min}^{ind})$ reaches its maximal value equal to $(\rho_{s,min}^{ind})^{-1}$. On the contrary, the

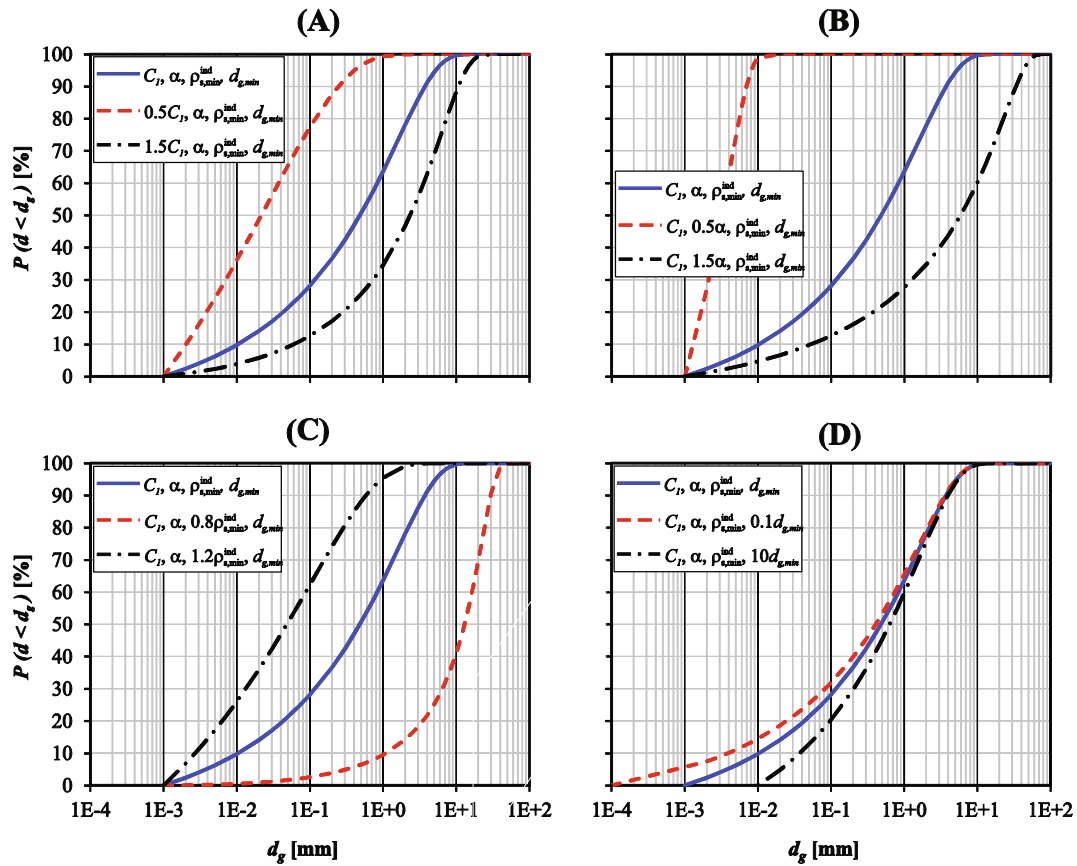


Fig. 3. Behavior of the proposed GSD model when changing values of: a) C_1 ; b) α ; c) $\rho_{s,min}^{ind}$; d) $d_{g,min}$. Initial parameter values (solid line in each graph) are $C_1 = 1.85 \times 10^{-2}$, $\alpha = 1.3$, $\rho_{s,min}^{ind} = 1.55$ and $d_{g,min} = 1 \times 10^{-3}$ mm.

lower resolution limit $\lambda_{low} = (\rho_{s,min}^{ind})^{1/\gamma_s}$ can be also computed from Eq. (6) for $\gamma(\lambda) = \gamma_s$, which is known as the most probable singularity:

$$\gamma_s = C_1 \alpha \left(\left(\frac{E}{C_1} \right)^{1/\alpha} - \frac{1}{\alpha} \right) \quad (8)$$

Note that Eq. (8) is derived from Eq. (2) given that $c(\gamma_s) = E$.

Finally, having on mind that $l(\lambda) = d_g$, and thus $\lambda = L / d_g$, the analytical GSD function can be derived by introducing Eqs. (7) into (4):

$$P(d < d_g) = 1 - \frac{\left(\frac{L}{d_g} \right)^{-c_1 \left(\frac{\ln(\rho_{s,min}^{ind})}{\ln(L/d_g)} + \frac{1}{\alpha} \right)}}{\left(\frac{L}{d_{g,min}} \right)^{-c_1 \left(\frac{\ln(\rho_{s,min}^{ind})}{\ln(L/d_{g,min})} + \frac{1}{\alpha} \right)}} \quad (9)$$

where $d_{g,min} = l(\lambda_n) = L / \lambda_n$ is the minimal grain diameter [L] equal to the size of a pixel at λ_n . From Eq. (9) the probability density function $p(d=d_g)$ can be derived as the first derivative of $P(d \geq d_g) = 1 - P(d < d_g)$ with respect to $\ln(L/d_g)$, providing the following expression:

$$p(d = d_g) = -c \left(\frac{L}{d_g} \right) \left(\frac{L}{d_{g,min}} \right)^c \left(\frac{L}{d_{g,min}} \right)^{-c} \left[1 - \frac{\ln(\rho_{s,min}^{ind})}{C_1} \right] e^{-c \left(\frac{L}{d_g} \right) \ln \left(\frac{L}{d_g} \right)} \quad (10)$$

where $c \left(\frac{L}{d_g} \right) = C_1 \left(\frac{\ln(\rho_{s,min}^{ind})}{\ln(L/d_g)} + \frac{1}{\alpha} \right)^\alpha$ is the co-dimension, while

$E - c \left(\frac{L}{d_g} \right)$ describes the change of fractal dimension with d_g . The approach proposed here would face certain issues mostly related to the way pixels are grouped. Therefore, it is possible to have λ_1^2 neighbor pixels that belong to a grain of larger size, but since they are distributed in different groups there is a “good” chance that this larger grain will not be recognized after the aggregation. On the contrary, those pixels can signify separated grains, but if they are aggregated as a part of the same group of λ_1^2 pixels, they will be recognized as a part of the larger grain. Nevertheless, these special cases do not influence the proposed algorithm significantly if applied on the sufficiently large λ .

2.2.1. Determination of the model parameters

Parameters of the proposed model (Eq. (9)) are: $d_{g,min}$, $\rho_{s,min}^{ind}$, α and C_1 . The first two are physical parameters whose values are either estimated based on the type of material ($d_{g,min}$), or calculated based on the experimentally determined values of ρ_{bulk} and $\rho_{s,min}$ (see Eq. (5)), while the last two (α and C_1) are statistical parameters determined by analyzing the scaling behavior of ρ^{ind} field. This is done by means of the

Trace Moment (TM) technique (Schertzer and Lovejoy, 1987) which assumes that the scaling of the average statistical moments of order p ($\langle (\rho^{ind}(\lambda))^p \rangle$) can be described through the moment scaling function $K(p)$:

$$\langle (\rho^{ind}(\lambda))^p \rangle \approx \lambda^{K(p)} \quad (11)$$

$$K(p) = \frac{C_1}{\alpha - 1} (p^\alpha - p); \alpha \neq 1 \quad (12)$$

where $K(p)$ is described through parameters C_1 and α (for more details see Schertzer and Lovejoy, 1987). Note that $c(\gamma)$ and $K(p)$ functions are linked by Legendre transform (Frisch and Parisi, 1985), meaning that for each γ there is a corresponding p (i.e. for $\gamma = C_1$ and $\gamma = \gamma_s$ the corresponding values are $p = 1$ and $p = p_s$, respectively).

To determine values of α and C_1 for a certain $\rho^{ind}(\lambda)$ field, the field is firstly up-scaled as previously described, and $\rho^{ind}(\lambda)$ values are raised on a power p at each λ . The average value of such a modified field ($\langle (\rho^{ind}(\lambda))^p \rangle$) is computed at each λ , and the procedure is repeated for variety of $p \geq 0$ values. After plotting $\log(\langle (\rho^{ind}(\lambda))^p \rangle)$ against $\log(\lambda)$, different linear regressions depending on p value are formed. Their slopes are related to $K(p)$ values that form the moment scaling function. Based on Eq. (12), the first derivative of the obtained $K(p)$ function at $p = 1$ is equal to $C_1 = \frac{dK(p)}{dp}|_{p=1}$ (calculated numerically), while the ratio between the second and the first derivative at $p = 1$ is $\alpha = \frac{1}{C_1} \frac{d^2K(p)}{dp^2}|_{p=1}$.

2.2.2. Influence of the model parameters

To better understand the influence of the four parameters on the model behavior, Eq. (9) has been tested on different values of each parameter, as illustrated in Fig. 3. For all cases presented in Fig. 3, value of $L = 100$ mm is kept constant while changing values of the four model parameters.

The impact of C_1 on the GSD is illustrated in Fig. 3a by increasing (dash-dotted line) / decreasing (dashed line) its initial value (solid line) by 50% while preserving values of the three remaining parameters. Similarly, in Fig. 3b value of α is changed by 50% in both ways. Fig. 3a shows that parameter C_1 mostly affects the break onto the finer particles and the shape of that part of the curve in a way that smaller C_1 secures higher contribution of fine grains (dashed line), while the case is opposite for higher C_1 (dash-dotted line). On the contrary, the change of parameter α (Fig. 3b) is less affecting the representation of small grains, but it is mainly responsible for the slope of the central part of the GSD curve, where smaller α provides steeper curve. Thus, in case of granular soils higher α and smaller C_1 values describe well-graded, while smaller α and higher C_1 describe more uniformly graded materials. Indeed, well-graded materials usually have lower total porosity due to the better spatial packing of grains, meaning the lower representation of zeros in ρ^{ind} field that causes stronger variability of the field (higher α) and lower intermittency of its mean value (lower C_1).

The impacts of $\rho_{s,min}^{ind}$ and $d_{g,min}$ on the GSD curve are also tested by varying one of the parameters while maintaining the rest. As illustrated in Fig. 3c, the higher $\rho_{s,min}^{ind}$ (more strict threshold value), the higher values of $P(d < d_g)$ (Eq. (9)), and vice versa. Unlike the three other parameters, $d_{g,min}$ dictates the total range of scales ($L/d_{g,min}$) by affecting mostly the distribution of small grains (tail of the GSD) - see Fig. 3d.

2.3. Soil sampling and image acquisition

In this section are given information about soil sampling and image acquisition for three different materials: Green Wave substrate and Horizons A and A20 of La Herreria soil.

2.4. Green Wave substrate

Green Wave substrate is an artificial coarse material (VulkaTec

Riebensahm GmbH, 2016) with 4% of organic matter, used for covering green roofs. Due to its volcanic nature (values of grain and dry bulk densities are 2.35 Mg/m³ and 1.42 Mg/m³, respectively), this material does not create a significant load on the roof construction which is the reason it has been used in case of Green Wave (Versini et al., 2018, 2020), a wavy shape green roof located next to Ecole des Ponts ParisTech in Champs-sur-Marne, France. The substrate contains 50% of grains larger than 1.6 mm, with 10% of particles between 10 and 20 mm in the coarse range, and 13% of fine particles smaller than 80 μ m. Distribution of grains larger than 80 μ m was determined by means of the dry sieving method (AFNOR, 1996), while the sedimentation test (AFNOR, 1992) was used for finer particles. The curvature and uniformity coefficients are $C_c = (D_{30})^2 / (D_{60} \times D_{10}) = 1.95$ and $C_u = D_{60} / D_{10} = 55$, respectively, and hence this substrate is regarded as well graded according to the ASTM D2487-06 (2006) standard.

The sample of the GW substrate (10 cm diameter and 15 cm height) was prepared by mixing and pouring the material into the plexiglass cylinder (compacted to in situ value of $\rho_{bulk} = 1.42$ Mg/m³), simulating the way substrate is placed on the roof to avoid segregation of fine particles at the bottom. Tomographic scans were conducted with a RX Solutions Ultratom microtomograph, including a Hamamatsu L10801 X-ray source and a Paxscan Varian 2520 V flat panel detector (1920 \times 1560 pix², pixel size 127 μ m). X-ray source tension and current were respectively 200 kV and 280 μ A. The detector was set at 4 fps, each projection resulting of an average over 25 projections, giving a total number of 4320 averaged projections. The sample being a long cylinder, stack mode was used and set to three turns. The reconstructed 3D image is finally represented by 1785 \times 1785 \times 3072 voxels with the edge length of 53.7 μ m.

2.5. La Herreria soil (Horizons A and A20)

Two intact samples (60 mm diameter and 100 mm height) of La Herreria soil were collected in the low land mountain area of Sierra de Guadarrama in Spain (Schmid et al., 2016), which is a highly degraded type of site because of the livestock keeping. One soil sample was extracted from the top 18 cm layer (Horizon A), being the result of biological alteration with roots resulting in fertile soil. This layer is moderately acid, with 2.5% of organic matter, 0.8% of Fe₂O₃, sandy texture (65% sand, 25% silt, 10% clay) and bulk density of 1.6 Mg/m³. The second soil sample was extracted from 18 to 40 cm depth (Horizon A20), also presenting an acid character (pH = 6) with 0.5% of organic matter, 0.7% of Fe₂O₃, 55%, 30% and 15% of sand, silt and clay particles, respectively, and bulk density of 1.7 Mg/m³.

X-ray CT scanning was performed using a Phoenix v | tome | x m 240 kV system (GE Sensing & Inspection Technologies GmbH, Wunstorf, Germany) at the Hounsfield Facility, University of Nottingham, UK. The scanner consisted of a 240 kV microfocus X-ray tube fitted with a tungsten reflection target and a DXR 250 digital detector array with 200 μ m pixel size (GE Sensing & Inspection Technologies GmbH, Wunstorf, Germany). A maximum X-ray energy of 140 kV and 200 μ A was used to scan the soil core. A total of 2400 projection images were acquired over a 360° rotation. Each projection was the average of six images acquired with a detector exposure time of 200 ms and the resulting isotropic voxel edge length was 32 μ m. The 3D image of the soil samples used in this work is represented by 676 \times 676 \times 300 voxels.

3. Results and discussion

The approach presented in this work is firstly validated on soil images of the GW substrate, and the experimental GSD data of the same material. Then, it is applied on two horizons of La Herreria soil, but in this case only measured percentages of sand, silt and clay particles were compared with model results because detailed GSD data are lacking. Finally, the comparison with the fractal-based PSF model (Perrier et al., 1999; Bird et al., 2000) is presented.

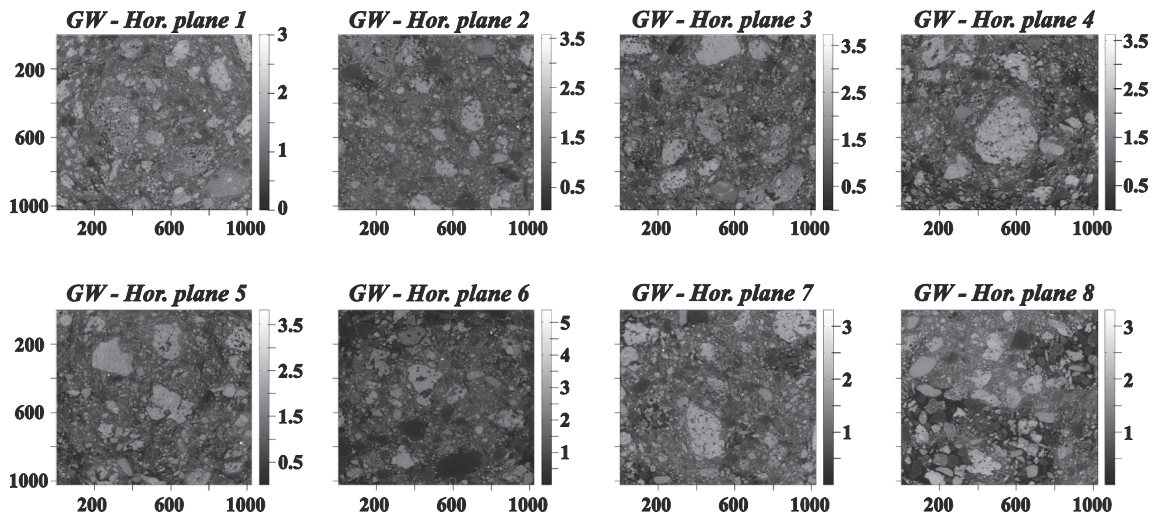
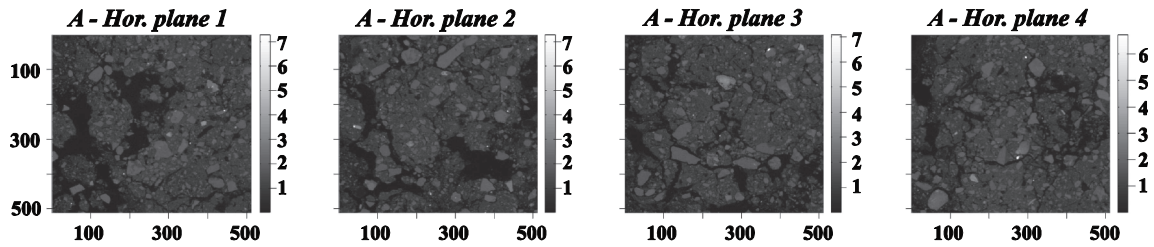


Fig. 4. Eight two-dimensional horizontal ρ^{ind} fields (1024 × 1024 pixels), extracted from the original three-dimensional grey scale image, that are equally distant along the specimen height.

(A) La Herreria - Horizon A



(B) La Herreria - Horizon A20

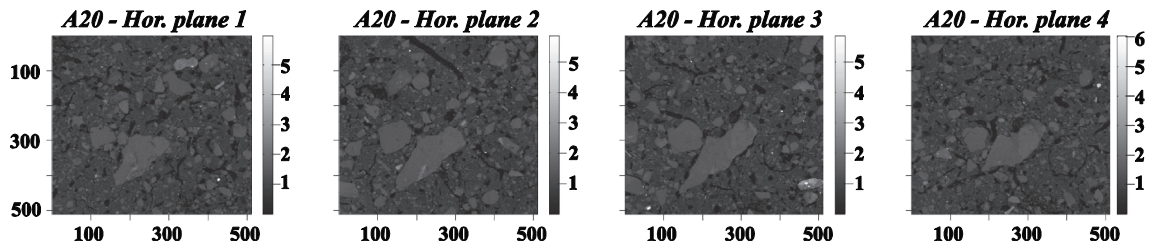


Fig. 5. a) Four equally distant horizontal ρ^{ind} fields (512 × 512 pixels) of Horizon A of La Herreria soil, extracted from the original three-dimensional grey scale image; b) same as in (a) just for Horizon A20.

3.1. Obtaining ρ^{ind} field by means of X-ray CT

The ρ^{ind} field is transformed from a grey-scale image carrying the information about different intensities of grey color - bright shades of grey represent high, and dark shades low density zones. Since grey-level intensities (GL) can be linked with density ρ by means of the linear regression (Taina et al., 2008), a linear correlation between ρ^{ind} [-] and original grey-level (GL) is obtained by:

- subtracting the GL_0 threshold value from the original GL values.
- setting to zero all GL values lower than GL_0 .
- renormalizing the modified GL field.

$$\rho^{ind} = \begin{cases} GL > GL_0, \frac{GL - GL_0}{\langle GL - GL_0 \rangle} \\ GL \leq GL_0, 0 \end{cases} \quad (13)$$

where notation $\langle \rangle$ indicates the mean value. GL_0 is adjusted based on the locations of pores that can be reliably identified on the image. By using Fiji (<https://fiji.sc/>), an open source Java-based image processing package, it was possible to estimate the value of GL_0 for all three materials.

In Fig. 4 are presented eight horizontal ρ^{ind} fields of the GW substrate extracted from the full-three dimensional scanned image. The resolution of the presented planes is 1024 x 1024 pixels ($\lambda_n = 2^{10}$), and they are equally distant in vertical direction (1.6 cm between two consecutive images). In Fig. 5A are presented four horizontal ρ^{ind} fields of La Herreria soil – Horizon A, while in Fig. 5B are presented horizontal fields of Horizon A20 (all images are 512 × 512 pixels - $\lambda_n = 2^9$).

3.2. UM model vs. Experimental data

The two-dimensional fields can be analyzed instead of the full-three

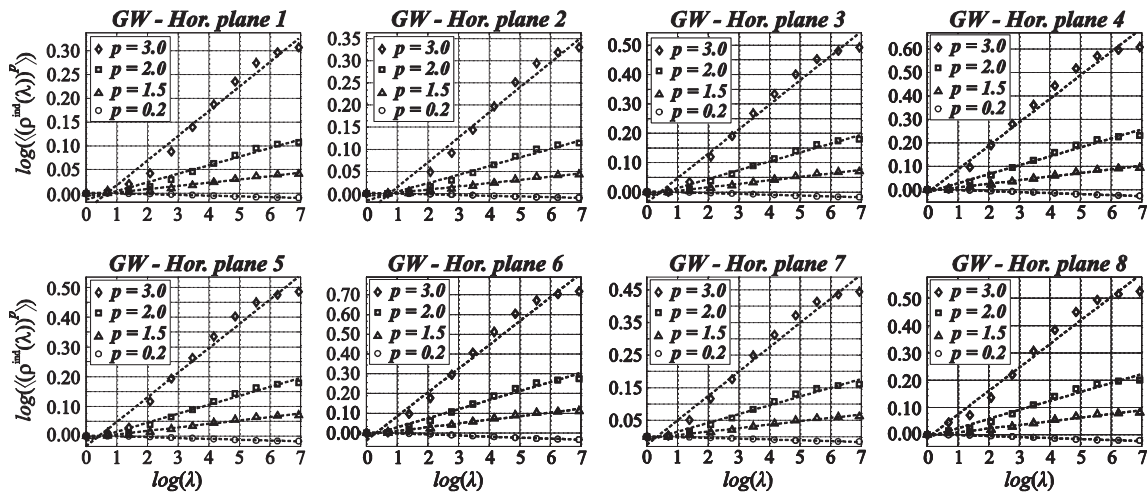
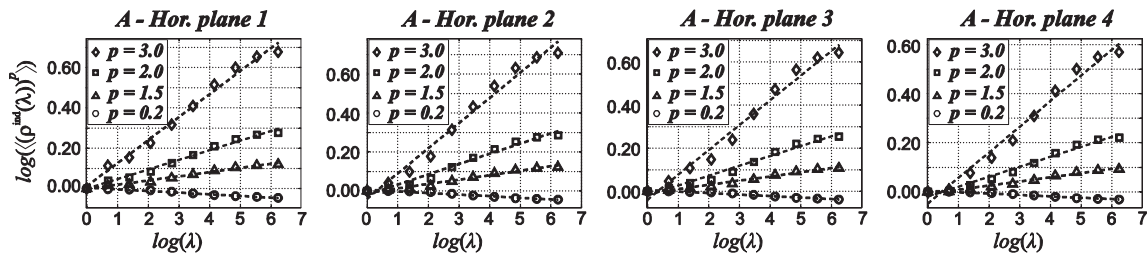


Fig. 6. Scaling of statistical moments of eight horizontal $\rho^{ind}(\lambda)$ fields of the GW substrate presented in Fig. 4.

(A) La Herreria - Horizon A



(B) La Herreria - Horizon A20

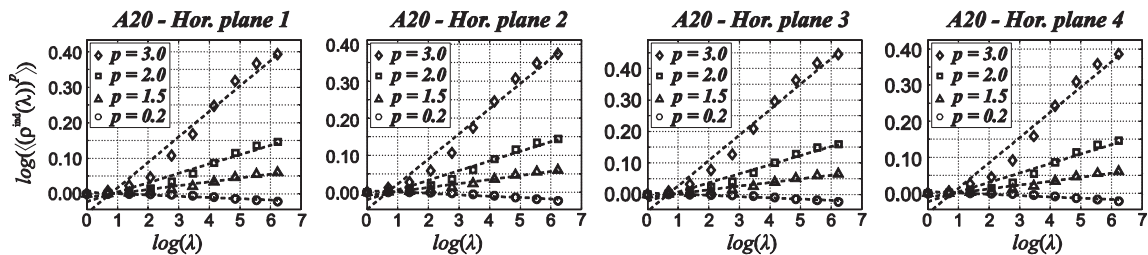


Fig. 7. a) Scaling of statistical moments of four horizontal $\rho^{ind}(\lambda)$ fields of La Herreria soil (Horizon A) presented in Fig. 5a; b) same as in (a) just for Horizon A20 (fields presented in Fig. 5b).

dimensional one only if the statistical isotropy within the soil specimen is secured, which is the case here (explained further in the text). Note that $\rho_{s,min}^{ind}$ and $d_{g,min}$ are physical properties of the particular material and they are considered as unique for the whole sample (and every two-dimensional slice within it), while α and C_1 are statistical parameters determined for every horizontal plane individually.

3.2.1. UM model parameters

In case of the GW substrate, value of $\rho_{s,min}^{ind}$ is computed as $\rho_{s,min}^{ind} = \frac{\rho_{s,min}}{\rho_{bulk}} = \frac{2.2}{1.42} = 1.55$, where $\rho_{s,min}$ and ρ_{bulk} are experimentally determined, while in case of La Herreria soils $\rho_{s,min}^{ind}$ values are adjusted to fit measured percentages of sand, silt and clay particles (explained later in the text) because the corresponding $\rho_{s,min}$ values are missing (only ρ_{bulk} values are given). Clearly, due to its physical basis, value of $\rho_{s,min}^{ind}$ should not change significantly regardless of the soil type (adjusted values are $\rho_{s,min}^{ind} = 1.73$ and 1.54 for Horizon A and A20, respectively).

Value of $d_{g,min}$ depends on the range of scales that is analyzed. If

focusing on the range of scales covered by the scanned image, $d_{g,min}$ corresponds to the pixel size at λ_n ($=1024$ and 512 for GW substrate and La Herreria soils, respectively), and thus it is equal to $d_{g,min} = L/\lambda_n \approx 60/1024 \approx 50 \mu m$ in case of the GW substrate, and $d_{g,min} = 16/512 \approx 32 \mu m$ for La Herreria soils. For the full-range of scales, $d_{g,min}$ represents the absolute minimal grain size that needs to be approximately estimated if not measured. For the GW substrate, $d_{g,min} = 1 \mu m$ is adopted based on the GW experimental data, while lower values of $d_{g,min} = 0.1 \mu m$ and $0.05 \mu m$ are adopted for Horizons A and A20 of La Herreria soil, respectively, having on mind significant percentages of clay particles in both cases (10% and 15%, respectively).

Finally, the UM parameters are determined by performing TM analysis on every $\rho^{ind}(\lambda)$ field presented in Fig. 4 and Fig. 5. In Fig. 6 is presented $\log((\rho^{ind}(\lambda))^p)$ versus $\log(\lambda)$ for four different p values (0.2, 1.5, 2 and 3) and eight horizontal $\rho^{ind}(\lambda)$ fields of the GW substrate presented in Fig. 4. In all cases, scaling of $\log((\rho^{ind}(\lambda))^p)$ (different symbols) can be reasonably well interpreted with linear regressions.

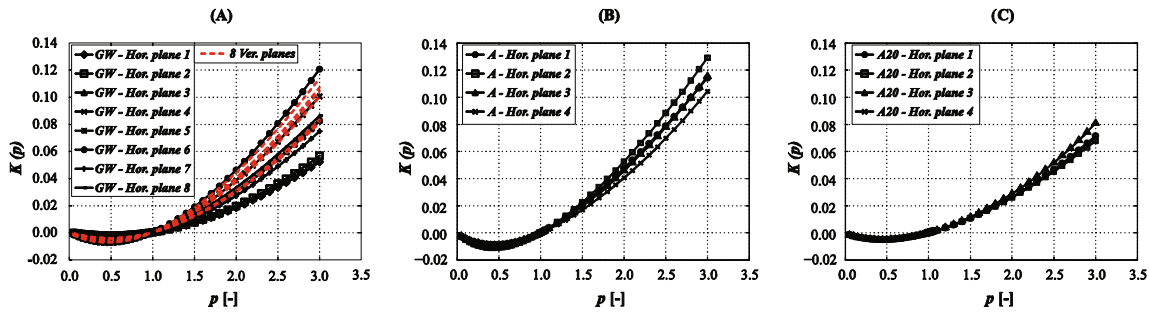


Fig. 8. Moment scaling functions $K(p)$ obtained by applying TM technique on: a) eight horizontal fields from Fig. 4 (different solid lines), and eight vertically oriented fields (dashed lines); b) four horizontal fields from Fig. 5a; c) four horizontal fields from Fig. 5b.

Table 1

Determined UM parameters for eight horizontal $\rho^{ind}(\lambda)$ fields of the GW substrate presented in Fig. 4, and eight vertical fields

Horizontal plane	1	2	3	4	5	6	7	8
C_1	9.34E-03	9.93E-03	1.64E-02	2.23E-02	1.66E-02	2.72E-02	1.45E-02	1.93E-02
α	1.93	1.96	1.83	1.67	1.80	1.61	1.85	1.66
Vertical plane	1	2	3	4	5	6	7	8
C_1	2.66E-02	2.21E-02	1.74E-02	1.72E-02	1.67E-02	1.63E-02	2.06E-02	2.37E-02
α	1.56	1.72	1.75	1.75	1.76	1.82	1.78	1.60

Table 2

Determined UM parameters for eight $\rho^{ind}(\lambda)$ fields of La Herreria soil (Horizons A and A20) presented in Fig. 5.

Horizon A	1	2	3	4
C_1	3.36E-02	3.55E-02	3.03E-02	2.60E-02
α	1.15	1.25	1.30	1.37
Horizon A20	1	2	3	4
C_1	1.62E-02	1.63E-02	1.73E-02	1.62E-02
α	1.46	1.40	1.48	1.44

This is also the case with La Herreria soils whose moment scaling behavior is illustrated in Fig. 7a for Horizon A, and in Fig. 7b for Horizon A20. The same kind of analysis is applied on the eight vertically oriented fields ($\lambda_n = 2^{10}$) of the GW substrate (equal horizontal distance between the two consecutive images). The quality of scaling is slightly better for vertical planes, but they are not presented in the Figure. Vertical planes for La Herreria soils were not analyzed since the maximal resolution of the vertically oriented image is 256 x 256 pixels ($\lambda_n = 2^8$), which is regarded as insufficient.

Based on the slopes of the obtained linear regressions, in Fig. 8 are presented $K(p)$ functions for all analyzed horizontal planes (different solid lines) of three different soils, together with $K(p)$ functions related

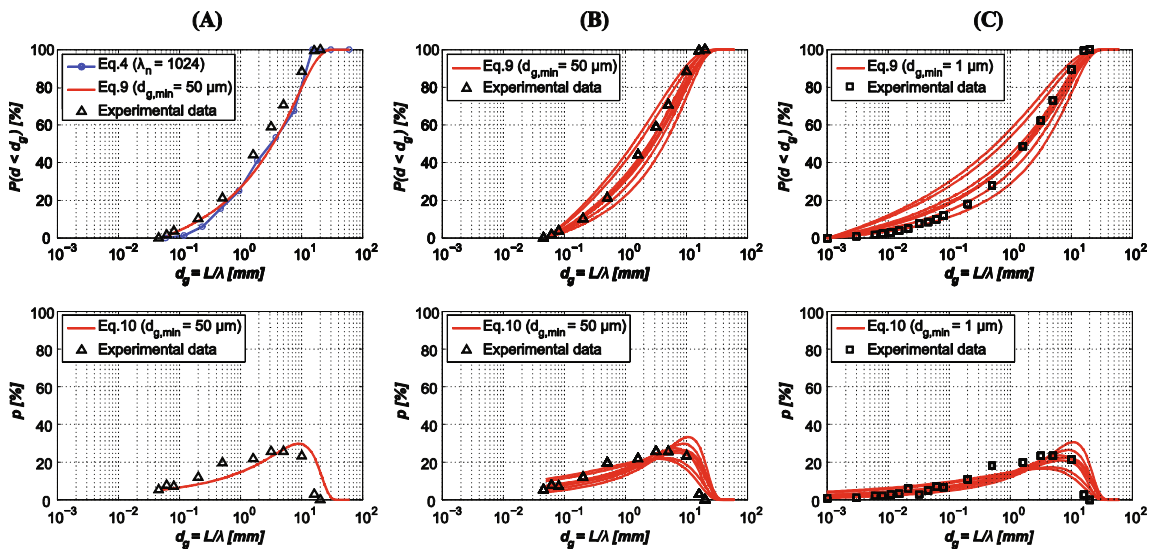


Fig. 9. Comparison between: a-top) Equation (9) applied on the GW Hor. plane 4 – solid line ($L = 60$ mm, $\rho_{s,min}^{ind} = 1.55$, $d_{g,min} = 50 \mu m$, $C_1 = 2.23 \times 10^{-2}$, $\alpha = 1.67$), Eq. (4) applied on the same field – connected dots ($\rho_{s,min}^{ind} = 1.55$, $\lambda_n = 1024$), and truncated experimental GSD data ($d_g \geq 50 \mu m$) - triangles; a-bottom) Equation (10) computed with the same parameter values as in a-top), and truncated experimental GSD data (triangles); b-top) Eq. (9) applied on eight $\rho^{ind}(\lambda)$ fields from Fig. 4 – solid lines (L , $\rho_{s,min}^{ind}$ and $d_{g,min}$ identical as in (a), α and C_1 presented in Table 1), and truncated experimental GSD data (triangles); b-bottom) Same as in a-bottom just for all fields from Fig. 4; c-top) Same as in b-top just for $d_{g,min} = 1 \mu m$ (solid lines), and full-range experimental GSD data ($d_g \geq 1 \mu m$) – squares; c-bottom) Same as in b-bottom just for $d_{g,min} = 1 \mu m$ (solid lines), and full-range experimental GSD data ($d_g \geq 1 \mu m$) – squares.

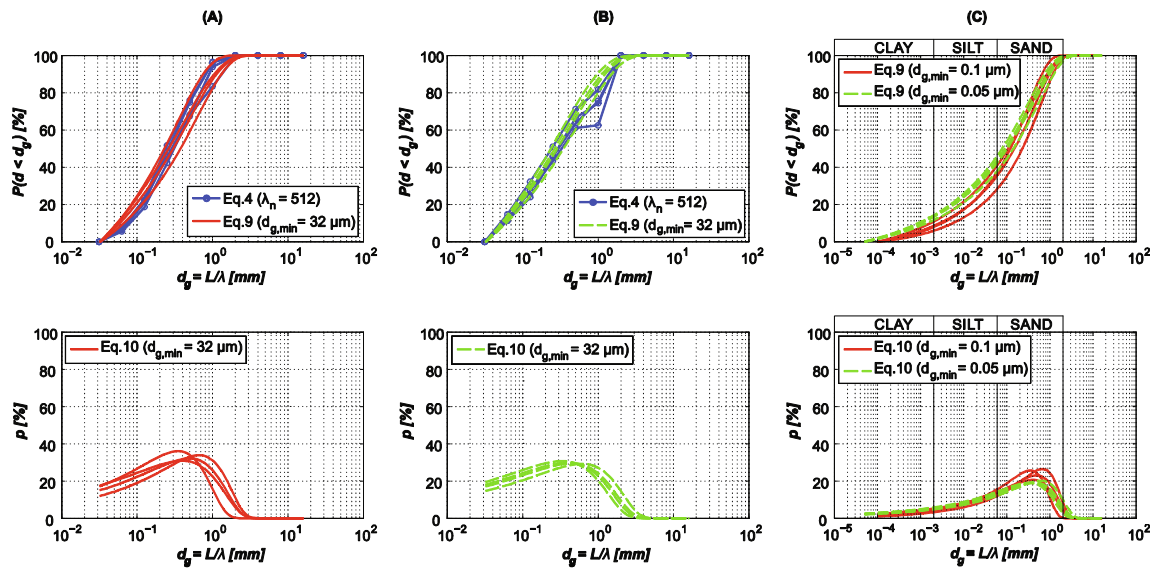


Fig. 10. Comparison between: a) Eq. (9) applied on four Horizon A fields from Fig. 5a ($L = 16$ mm, $\rho_{s,min}^{ind} = 1.73$, $d_{g,min} = 32$ μm , α and C_1 from Table 2), and Eq. (4) (box-counting method) applied on same fields ($\lambda_n = 512 \approx L/d_{g,min}$); b) Same as in (a) just for Horizon A20 ($\rho_{s,min}^{ind} = 1.54$); c) Eq. (9) applied on four fields from Fig. 5a (parameters same as in (a), only $d_{g,min} = 0.1$ μm – solid lines) and on four fields from Fig. 5b (parameters same as in (b), only $d_{g,min} = 0.05$ μm – dashed lines). In all three cases bottom graphs are obtained by means of Eq. (10) using the corresponding parameter values.

to the vertical planes of the GW substrate (dashed lines in Fig. 8a). Since vertical and horizontal $K(p)$ functions are overlapping in case of the GW substrate, indicating similar values of α and C_1 (see Table 1), it is reasonable to assume the statistical isotropy within the GW specimen. Even though vertical images are not analyzed, the same assumption is adopted for two remaining soils, having on mind the obtained horizontal $K(p)$ functions are rather similar (values of α and C_1 are presented in Table 2).

Low values of C_1 (order of magnitude 10^{-2}) obtained for all three soils indicate the narrow range of ρ^{ind} values, meaning that ρ cannot be significantly larger than ρ_{bulk} (should be the case regardless of the soil type). Also, higher α values (closer to 2) point out more significant fluctuations of ρ around ρ_{bulk} , indicating the presence of different grain sizes with different densities.

3.2.2. Comparison with experimental data

After determining values of the four model parameters, Eq. (9) is firstly tested on the ρ^{ind} field of the Hor. plane 4 of the GW substrate (see Fig. 4). Since focusing on the range of scales covered by the image, $d_{g,min} = 50$ μm is used. Fig. 9a-top illustrates comparison between Eq. (9) (UM model - solid line), Eq. (4) (connected dots) that uses the counted number of $\rho^{ind}(\lambda) \geq \rho_{s,min}^{ind}$ values at different λ , and the truncated experimental GSD data of the GW substrate (triangles). In Fig. 9a-bottom are compared probability density functions coming from the UM model (Eq. (10) – solid lines) and measurements (triangles). Good agreement between different analytical curves and truncated experimental data that consider only $d_g \geq 50$ μm is obtained.

In Fig. 9b-top is presented comparison between the same truncated experimental data (triangles) and Eq. (9) applied on every ρ^{ind} field of Fig. 4 (different solid lines), while in Fig. 9b-bottom are illustrated the corresponding probability density functions (Eq. (10)).

Finally, in Fig. 9c-top and Fig. 9c-bottom the full range experimental data (squares) are compared with Eqs. (9) and (10), respectively, by using the same parameter values as in Fig. 9b, with only difference that $d_{g,min} = 1$ μm is adopted. The agreement between the Eqs. (9) / (10) and both truncated and full-range experimental data is considered as satisfactory. The obtained family of curves creates reasonably narrow confidential zone around experimental points, verifying that way the analytical model proposed.

In Fig. 10 is presented the same kind of analysis as in Fig. 9, but for Horizons A and A20 of La Herreria soil. In Fig. 10a and b are illustrated results obtained from ρ^{ind} fields of Fig. 5a (Horizon A) and Fig. 5b (Horizon A20), respectively, where $d_{g,min} = 32$ μm is adopted, while in Fig. 10c are compared full-range results for Horizon A (solid lines) and Horizon A20 (dashed lines) using $d_{g,min} = 0.1$ μm and $d_{g,min} = 0.05$ μm , respectively. As mentioned earlier in the text, values of $\rho_{s,min}^{ind}$ (1.73 and 1.54 for Horizons A and A20, respectively) are adjusted so that the average percentages of sand, silt and clay particles, computed based on the model results from Fig. 10c, fit well with measured values. For Horizon A, the average computed values of sand, silt and clay particles are 64%, 27% and 8% (about 1% of particles greater than 2 mm), respectively, while for Horizon A20 those values are 54%, 32% and 14%, respectively. The results obtained with a model are rather close to measurements, confirming the UM model is valid.

The proposed UM approach was successfully evaluated on soils that cover wide range of grain sizes with significant percentages of both coarse and fine particles. To see limitations of the model, it was additionally tested on a material with a rather uniform GSD curve, the Hostun sand HN31 extracted in the Drôme region in France (Bruchon et al., 2013). This sand is made of about 98% of quartz (grain densities are uniform), and it covers rather narrow spectrum of grain sizes (0.2 ÷ 0.8 mm). Preliminary results showed the proposed approach is not applicable on such material, having on mind the scaling of statistical moments in log–log scale significantly deviates from linear regression, and hence parameters α and C_1 cannot be determined.

3.3. UM model vs. PSF model

The PSF approach, a three-phase fractal-based GSD model firstly introduced by Perrier et al. (1999), is also used for interpreting the experimental GSD curve of the GW substrate. According to this model, the GSD can be described using the following expression (Bird et al., 2000):

$$P(d < d_g) = \left(\frac{d_g}{d_{g,max}} \right)^{3-D_{f,PSF}} \quad (14)$$

where $D_{f,PSF}$ is the fractal coefficient [–] whose optimal value can be determined from the slope of the best fitting linear regression in

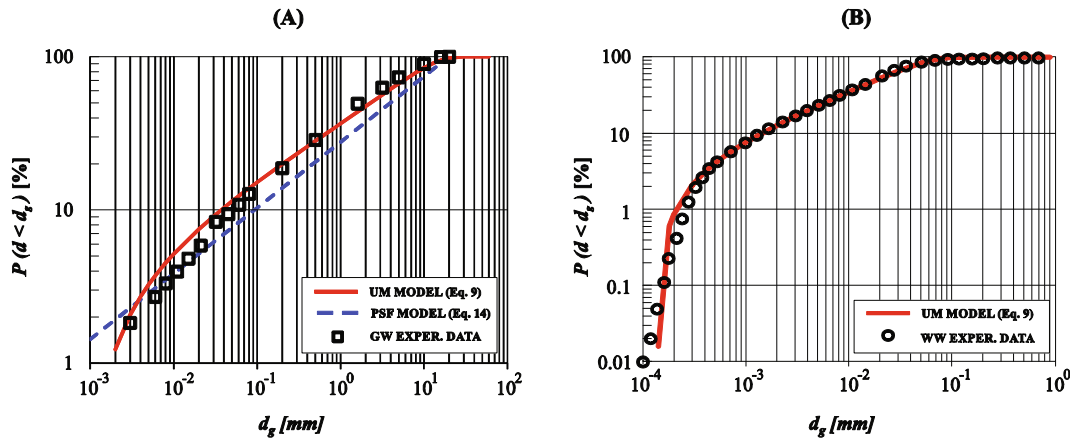


Fig. 11. a) Comparison between the experimental GSD data of the GW substrate (squares) and Eq. (9) (solid lines) and (14) (dashed lines) computed with the adjusted parameter values that fit the measurements ($C_1 = 2.25 \times 10^{-2}$ and $\alpha = 1.60$ for UM model, and $D_{f,PSF} = 2.57$ for PSF model); b) same as in (a) just for Walla Walla soil taken from Bittelli et al. (1999) – $L = 1$ mm, $d_{g,min} = 1 \times 10^{-4}$ mm, $\rho_{s,min}^{ind} = 1.72$, $\alpha = 1.05$, $C_1 = 4.5 \times 10^{-2}$ (PSF model is not illustrated since it clearly deviates from the measurements).

logarithmic scale that goes through the experimental GSD data and reaches 100% at $d_{g,max}$. By adopting $d_{g,max} = 18$ mm in case of the GW substrate, the optimal value of $D_{f,PSF} = 2.57$ is obtained (dashed line in Fig. 8a).

To better illustrate the difference between the PSF (Eq. (14)) and the UM model (Eq. (9)), probability functions are presented in a log–log scale (Fig. 11a). For the same values of L , $d_{g,min}$ and $\rho_{s,min}^{ind}$ as in Fig. 9c, the best agreement between Eq. (9) and measurements is obtained for $\alpha = 1.60$ and $C_1 = 2.25 \times 10^{-2}$. These values are rather close to those describing the horizontal plane 4 of the GW substrate (see Table 1), confirming the physical basis of the proposed approach.

To test whether the UM model can be used for soils with multi-modal GSD curves that are described with multiple fractal dimensions, Eq. (9) is compared with experimental data of Walla Walla (WW) soil, described in Bittelli et al. (1999) by means of three different fractal dimensions related to distributions of sandy, silty and clayey particles. According to the U.S. soil taxonomy, this soil is Typic Haploxeroll with 8.3% of sand, 78.4% of silt and 13.3% of clay. Due to the lack of scanned soil images and other relevant information, the UM model parameters could not be determined as explained earlier in the text, but only roughly estimated / adjusted. Fig. 11b shows that for $\rho_{s,min}^{ind} = 1.72$, $\alpha = 1.05$, $C_1 = 4.5 \times 10^{-2}$, and $L/d_{g,min} = 1$ mm/ 1×10^{-4} mm (from the graph), Eq. (9) provides rather good agreement with WW experimental points. Since the relevant information are missing, these results should be taken with a grain of salt and understood only as a test if the model is capable of interpreting multi-modal GSD curves.

Compared to Eq. (14) which considers the fixed fractal dimension $D_{f,PSF}$, Eq. (9) takes into account the fractal dimension that changes with d_g (the co-dimension function). Therefore, for the UM approach it is quite important to know the total range of scales investigated ($L/d_{g,min}$). Even though the PSF model (Eq. (14)) is more convenient for practical application, since it uses only two parameters that can be determined quite easily, the UM model proposed in this work (Eqs. (9) and (10)) shows better agreement with experimental GSDs for soils with wide spectrum of grain sizes whose distribution cannot be accurately described with a simple fractal (power) law.

4. Conclusion

This work shows that the up-scaling approach presented can be used for predicting the GSD of a certain material based on its scanned micro-structure which represents a density indicator field. By reducing the resolution of the scanned image, density indicator values above the fixed threshold are treated at each resolution as a cumulative representation

of solid particles of diameter equal to or larger than the corresponding pixel size. The quantity of values above the threshold at different resolutions can be analytically described by means of the Universal Multifractals (UM), leading to the new multifractal-based GSD model. The model uses four parameters, where two of them are physical (the minimal grain diameter and the ratio between the minimal grain density and dry bulk density), while the other two are statistical UM parameters that characterize the spatial heterogeneity of the soil density field.

An innovative approach proposed in this work was tested on three different materials containing significant percentages of both coarse and fine particles: an unconventional volcanic granular material used for covering green roofs, and two horizons of La Herreria soil collected from the low land mountain area of Sierra de Guadarrama in Spain. By performing the Trace Moment analysis on two-dimensional scanned soil images (density indicator field) of different materials, the statistical parameters (C_1 and α) were determined and families of analytical GSD curves were obtained for each material, showing a good agreement with experimental data. Additionally, the UM approach was tested on Houston quartz sand and results showed that such a uniform GSD cannot be reliably estimated by means of the presented methodology. In all cases, the analysis was applied on two-dimensional images to save computational time and memory, which is legit if the statistical isotropy within the specimen is secured.

Results showed the values of C_1 are the same order of magnitude for different soils (10^{-2}) because density of an individual grain cannot be significantly larger than the dry bulk density, regardless of the soil type. Also, it was proved that lower C_1 and higher α are related to GSD curves that change gradually with respect to grain sizes, while lower α and higher C_1 are related to the steeper GSD curve in its central part and stronger curvature close to the break onto the finer particles.

Finally, the proposed four parameters UM model was compared with the fractal-based two parameters PSF model, showing better agreement with the Green Wave experimental data. Its advantage was additionally emphasized by showing excellent agreement with multi-modal GSD curve of Walla Walla soil that is described in the literature by means of three different fractal dimensions related to sandy, silty and clayey particles.

Declaration of Competing Interest

The authors declare that they have no known competing financial interests or personal relationships that could have appeared to influence the work reported in this paper.

Acknowledgment

Authors greatly acknowledge the Research Direction of Ecole des

Ponts ParisTech, who provided Inter laboratory PhD Merit Scholarship to the first author.

Appendix: Analogy between the up-scaling approach and the dry sieving method

The analogy between Eq. (4) (the up-scaling approach) and the dry sieving method can be derived under the following assumptions:

1. Three-dimensional space is considered ($E = 3$) since the dry sieving method is based on the grain masses.
2. All grains have the same shape and density ρ_s .
3. A discrete number of sieves is used, and hence the size of voids on each sieve follows the size of voxels $l(\lambda_{n-i})$ at different λ_{n-i} where $i = [0 \div n]$.

The total mass of the specimen (M_{total}) is placed on the cascade of sieves arranged in a descending order (the largest void size is on the top, while the smallest one is on the bottom). If all grains are distributed on the corresponding sieves $i = [0 \div n]$, it can be assumed that those staying on a certain sieve have diameter equal to the size of sieve voids. Therefore, the following can be written for $i = 0$:

$$M(d \geq l(\lambda_n)) = M_{total} = C_V \rho_s \sum_{j=0}^n N_g(\lambda_{n-j}) l(\lambda_{n-j})^3 \quad (A1)$$

where C_V is the volume shape coefficient [-] (for cube $C_V = 1$, for sphere $C_V = \pi/6$), $N_g(\lambda_{n-j})$ is the number of grains [-] that stay on the sieve of void size $l(\lambda_{n-j})$ [L] ($j = 0 \div n$). Since grains that stay on the sieve $l(\lambda_n)$ are assumed to have identical diameters, $l(\lambda_n)^3$ can be pulled outside the sum, and the following is obtained:

$$M(d \geq l(\lambda_n)) = C_V \rho_s l(\lambda_n)^3 \sum_{j=0}^n N_g(\lambda_{n-j}) \left(\frac{l(\lambda_{n-j})}{l(\lambda_n)} \right)^3 \quad (A2)$$

$$N_g^{cum}(\lambda_n) \approx C_V \sum_{j=0}^n N_g(\lambda_{n-j}) \left(\frac{l(\lambda_{n-j})}{l(\lambda_n)} \right)^3 \quad (A3)$$

where $N_g^{cum}(\lambda_n)$ is the cumulative number of grains equal to or larger than $d_{g,min} = l(\lambda_n)$. Following Eq. (A2), the cumulative mass of all grains equal to or larger than $l(\lambda_{n-i})$ can be expressed as the following:

$$M(d \geq l(\lambda_{n-i})) = C_V \rho_s l(\lambda_{n-i})^3 \sum_{j=i}^n N_g(\lambda_{n-j}) \left(\frac{l(\lambda_{n-j})}{l(\lambda_{n-i})} \right)^3 \quad (A4)$$

$$N_g^{cum}(\lambda_{n-i}) \approx C_V \sum_{j=i}^n N_g(\lambda_{n-j}) \left(\frac{l(\lambda_{n-j})}{l(\lambda_{n-i})} \right)^3 \quad (A5)$$

By introducing Eqs. (A3) into (A2) and (A5) into (A4), and having on mind that $d_g = l(\lambda_{n-i})$, the GSD can be expressed as:

$$P(d < d_g) = 1 - \frac{M(d \geq l(\lambda_{n-i}))}{M(d \geq l(\lambda_n))} \quad (A6)$$

$$P(d < d_g) = 1 - \frac{N_g^{cum}(\lambda_{n-i})}{N_g^{cum}(\lambda_n)} \left(\frac{l(\lambda_{n-i})}{l(\lambda_n)} \right)^3 \quad (A7)$$

Note that $N_g^{cum}(\lambda_{n-i})$ and $N_g^{cum}(\lambda_n)$ correspond to $N(\rho^{ind}(\lambda) \geq \rho_{s,min}^{ind})$ and $N(\rho^{ind}(\lambda_n) \geq \rho_{s,min}^{ind})$ in Eq. (4), respectively, while $\frac{l(\lambda_{n-i})}{l(\lambda_n)} = \frac{\lambda_n}{\lambda_{n-i}}$. Therefore, Eq. (A7) is identical to Eq. (4) for $E = 3$, just in a discrete form.

References

- AFNOR, 1992. Analyse Granulométrique Des Sols - Méthode Par Sédimentation. Association Française de Normalisation, France.
- AFNOR, 1996. Analyse Granulométrique - Méthode Par Tamisage à Sec Après Lavage. Association Française de Normalisation, France.
- ASTM International. 2006. Standard Practice for Classification of Soils for Engineering Purposes (Unified Soil Classification System). ASTM D2487-06(2006). West Conshohocken, PA: ASTM International, approved May 1, 2006. 10.1520/D2487-06.
- Banhart, J., 2008. Advanced Tomographic Methods in Materials Research and Engineering. Oxford University Press, New York.
- Beuselinck, L., Govers, G., Poesen, J., Degraer, G., Froyen, L., 1998. Grainsize analysis by laser diffractometry: Comparison with the sieve-pipette method. Catena 32 (3-4), 193-208. [https://doi.org/10.1016/S0341-8162\(98\)00051-4](https://doi.org/10.1016/S0341-8162(98)00051-4).
- Bird, N.R.A., Perrier, E., Rieu, M., 2000. The water retention function for a model of soil structure with pore and solid fractal distributions. Eur. J. Soil Sci. 51 (1), 55-63. <https://doi.org/10.1046/j.1365-2389.2000.00278.x>.
- Bittelli, M., Campbell, G.S., Flury, M., 1999. Characterization of particle-size distribution with a fragmentation model. Soil Sci. Soc. Am. J. 63, 782-788.
- Bruchon, J.F., Pereira, J.M., Vandamme, M., Lenoir, N., Delage, P., Bornert, M., 2013. Full 3D investigation and characterisation of capillary collapse of a loose unsaturated sand using X-Ray CT. Granular Matter. 15 (6), 783-800. <https://doi.org/10.1007/s10035-013-0452-6>.
- Frisch, U., Parisi, G., 1985. A multifractal model of intermittency. Turbulence Predictability in Geophysical Fluid Dynamics Climate Dynamics. 84-88.
- Ghanbarian-Alavijeh, B., Millán, H., Huang, G., 2011. A review of fractal, prefractal and pore-solid-fractal models for parameterizing the soil water retention curve. Can. J. Soil Sci. 91 (1), 1-14. <https://doi.org/10.4141/cjss10008>.
- Ghanbarian, B., Hunt, A.G., 2017. Fractals - Concepts and Applications in Geoscience. CRC Press, Boca Raton.
- Grout, H., Tarquis, A.M., Wiesner, M.R., 1998. Multifractal analysis of particle size distributions in soil. Environ. Sci. Technol. 32 (9), 1176-1182. <https://doi.org/10.1021/es9704343>.
- He, D., Ekere, N. N., Cai, L. 1999. Computer Simulation of Random Packing of Unequal Particles. Physical Review E. 60 (6), 7098-7104. <http://www.ncbi.nlm.nih.gov/pubmed/11970649>.
- Hsieh, J., 2003. Computed Tomography: Principles, Design, Artifacts, and Recent Advances, 114th ed. Society of Photo Optical.

- Lai, Z., Chen, Q., 2019. Reconstructing granular particles from X-Ray Computed Tomography Using the TWS Machine Learning Tool and the Level Set Method. *Acta Geotechnica* 14 (1), 1–18. <https://doi.org/10.1007/s11440-018-0759-x>.
- Martín, M.A., Montero, E., 2002. Laser diffraction and multifractal analysis for the characterization of dry soil volume-size distributions. *Soil and Tillage Research* 64 (1–2), 113–123. [https://doi.org/10.1016/S0167-1987\(01\)00249-5](https://doi.org/10.1016/S0167-1987(01)00249-5).
- Miller, B.A., Schaetzl, R.J., 2012. Precision of soil particle size analysis using laser diffractometry. *Soil Sci. Soc. Am. J.* 76 (5), 1719–1727. <https://doi.org/10.2136/sssaj2011.0303>.
- Nolan, G.T., Kavanagh, P.E., 1993. Computer simulation of random packings of spheres with log-normal distributions. *Powder Technol.* 76 (3), 309–316. [https://doi.org/10.1016/S0032-5910\(05\)80012-9](https://doi.org/10.1016/S0032-5910(05)80012-9).
- Perrier, E., Bird, N., Rieu, M., 1999. Generalizing the fractal model of soil structure: The pore-solid fractal approach. *Develop. Soil Sci.* 27, 47–74. [https://doi.org/10.1016/S0166-2481\(00\)80005-7](https://doi.org/10.1016/S0166-2481(00)80005-7).
- Posadas, A.N.D., Giménez, D., Bittelli, M., Vaz, C.M.P., Flury, M., 2001. Multifractal characterization of soil particle-size distributions. *Soil Sci. Soc. Am. J.* 65 (5), 1361–1367. <https://doi.org/10.2136/sssaj2001.6551361x>.
- Schertzer, D., Lovejoy, S., 1987. Physical modeling and analysis of rain and clouds by anisotropic scaling multiplicative processes. *J. Geophys. Res.* 92, 9693–9714.
- Schertzer, D., Lovejoy, S., 1997. Universal Multifractals Do Exist!: Comments on ‘A statistical analysis of mesoscale rainfall as a random cascade’. *J. Appl. Meteorol.* 36, 1296–1303.
- Schmid, T., Inclán-Cuarteras, R.M., Santolaria-Canales, E., Saa, A., Rodríguez-Rastrero, M., Tanarro-García, L.M., Luque, E., Pelayo, M., Ubeda, J., Tarquis, A.M., Díaz-Puente, J. De, Marcos, J., Rodríguez-Alonso, J., Hernández, C., Palacios, D., Gallardo-Díaz, J., González-Rouco, J.F., 2016. In Proceedings of the EGU General Assembly Conference Abstracts.
- Segal, E., Shouse, P.J., Bradford, S.A., Skaggs, T.H., Corwin, D.L., 2009. Measuring particle size distribution using laser diffraction: Implications for predicting soil hydraulic properties. *Soil Sci.* 174 (12), 639–645. <https://doi.org/10.1097/SS.0b013e3181c2a928>.
- Stanić, F., Cui, Y.-J., Delage, P., De Laure, E., Versini, P.-A., Schertzer, D., Tchiguirinskaia, I., 2019. A Device for the Simultaneous Determination of the Water Retention Properties and the Hydraulic Conductivity Function of an Unsaturated Coarse Material; Application to a Green-Roof Volcanic Substrate. *Geotechnical Testing J.* 43 (3), 547–564. <https://doi.org/10.1520/GTJ20170443>.
- Stanić, F., Delage, P., Cui, Y.-J., De Laure, E., Versini, P.-A., Schertzer, D., Tchiguirinskaia, I., 2020b. Two Improvements to Gardner’s method of measuring the hydraulic conductivity of non-saturated media: Accounting for impedance effects and non-constant imposed suction Increment. *Water Resour. Res.* 56, 1–15. <https://doi.org/10.1029/2019WR026098>.
- Taina, I.A., Heck, R.J., Elliot, T.R., 2008. Application of X-Ray Computed Tomography to Soil Science: A literature review. *Can. J. Soil Sci.* 88, 1–20.
- Torre, I.G., Losada, J.C., Tarquis, A.M., 2016. Multiscaling properties of soil images. *Biosyst. Eng.* 168, 133–141. <https://doi.org/10.1016/j.biosystemseng.2016.11.006>.
- Versini, P.-A., Gires, A., Fitton, G., Tchiguirinskaia, I., Schertzer, D., 2018. Toward an Assessment of the hydrological components variability in green infrastructures: pilot site of the green wave (Champs-Sur-Marne). *La Houille Blanche.* 104 (4), 34–42. <https://doi.org/10.1051/lhb/2018040>.
- Versini, P.-A., Stanić, F., Gires, A., Schertzer, D., Tchiguirinskaia, I., 2020. Measurements of the Water Balance Components of a Large Green Roof in the Greater Paris Area. *Earth Syst. Sci. Data.* 12, 1025–1035. <https://doi.org/10.5194/essd-12-1025-2020>.
- VulkaTec Riebenschahm GmbH. 2016. “Vulkaplus intensiv 0/12 / Vulkaplus Intensiv Typ Leicht.” http://web.archive.org/web/20190423142633/http://www.vulkatec.de/Begrueenung/Dachbegrueenung/Intensivbegrueenung-bei-Substratstaerken-bis-50cm/Vulkaplus-Intensiv-0_12/?&d=1.